Journal of Power Sources 220 (2012) 317–323

Contents lists available at SciVerse ScienceDirect

Journal of Power Sources

journal homepage: www.elsevier.com/locate/jpowsour

Hydrothermal synthesis of morphology-controlled $LiFePO_4$ cathode material for lithium-ion batteries

Bo Pei [a,b], Hongxu Yao [a,b], Weixin Zhang [a,b,*], Zeheng Yang [a,b]

[a] School of Chemical Engineering, Hefei University of Technology, Hefei, Anhui 230009, PR China
[b] Anhui Key Laboratory of Controllable Chemical Reaction & Material Chemical Engineering, Hefei, Anhui 230009, PR China

HIGHLIGHTS

- An SDBS-mediated hydrothermal method is used to prepare morphology-controlled $LiFePO_4$.
- $LiFePO_4$ morphology evolves from nanorod to nanoplate by adjusting the SDBS concentration.
- $LiFePO_4$/C nanoplates with shorter b-axis have superior electrochemical performance.

GRAPHICAL ABSTRACT

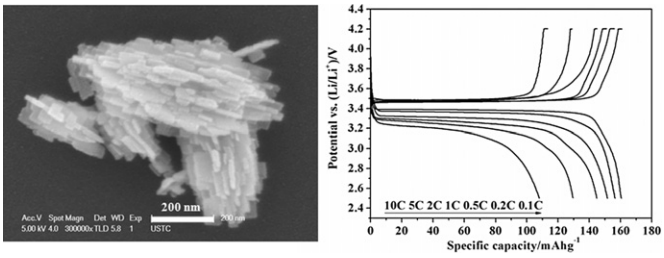

ARTICLE INFO

Article history:
Received 4 April 2012
Received in revised form
4 June 2012
Accepted 31 July 2012
Available online 9 August 2012

Keywords:
Lithium-ion batteries
Lithium iron phosphate
Hydrothermal synthesis
Sodium dodecyl benzene sulfonate
Electrochemical performance

ABSTRACT

A simple sodium dodecyl benzene sulfonate (SDBS) mediated hydrothermal method has been described in this paper to prepare morphology-controlled $LiFePO_4$, cathode material such as nanoparticles, nanorods and nanoplates with controllable b-axis thickness. When used in lithium-ion batteries, the $LiFePO_4$/C nanoparticles (200 nm in size) and nanorods (90 nm in diameter along b-axis and 200 nm–1 μm in length) display initial discharge capacities of 145.3 and 149.0 mAh g^{-1} at 0.1 C rate, 33.9 and 61.3 mAh g^{-1} at 10 C rate, respectively. The $LiFePO_4$/C nanoplates (20 nm thickness along b-axis and 50 nm width) deliver a discharge capacity of 162.9 mAh g^{-1} at 0.1 C rate and 107.9 mAh g^{-1} at 10 C rate. The Li-ion diffusion coefficients of the $LiFePO_4$/C nanoparticles, nanorods and nanoplates are calculated to be 1.66×10^{-12}, 2.99×10^{-12} and 1.64×10^{-11} cm^2 s^{-1}, respectively. In general, the discharge capacity and rate performance have been found to increase with the decreasing thickness of the b-axis. The experimental results demonstrate that decreasing the crystallite size in the b-axis and increasing the surface area of (010) plane can shorten Li-ion diffusion path and increase the electrode reaction, which significantly improve electrochemical performance of the $LiFePO_4$/C nanocomposites.

1. Introduction

Recently, there has been an increasing demand for higher performance and cheaper rechargeable batteries in different electronic devices. Since lithium iron phosphate was first reported as a cathode material for rechargeable lithium batteries in 1997 [1], extensive studies have focused on olivine-structured $LiFePO_4$ materials due to its low cost, non-toxicity, environmental safety, cycling stability [2], high theoretical capacity (170 mAh g^{-1}) [3] and charge–discharge potential (3.45 V versus Li^+/Li). However, a separation of the FeO_6 octahedra by PO_4^{3-} ions in the $LiFePO_4$ structure reduces its electronic conductivity, and a slightly distorted hexagonal close-packed oxygen array provides limited channels for Li-ion diffusion [1]. The poor electronic conductivity and slow diffusion of lithium ions [4,5] impede rate capability, a critical parameter for high power applications [6,7].

* Corresponding author. School of Chemical Engineering, Hefei University of Technology, Tunxi Road 193#, Hefei, Anhui 230009, PR China. Tel./fax: +86 551 2901450.
E-mail address: wxzhang@hfut.edu.cn (W. Zhang).

0378-7753/$ – see front matter © 2012 Elsevier B.V. All rights reserved.
http://dx.doi.org/10.1016/j.jpowsour.2012.07.128

In this context, tremendous efforts have been made in recent years to overcome these problems in three aspects: enhancing the surface electron conductivity (by conductive agent coating) [3,8,9]; increasing Li-ion conductivity in the bulk (by cationic doping) [10,11]; and especially decreasing the Li-ion transport path (by reducing the particle size) [12]. Isam et al. [13] reported that the Li^+ ions preferably move along b-axis rather than along the a- or c-axis in crystals with the orthorhombic space group *Pnma* due to the lowest Li^+ migration energy. Gaberscek et al. [14] presented a theoretical model to explain why the ionic conductivity (ca. 10^{-11}–10^{-10} S cm^{-1} at RT) of $LiFePO_4$ is much smaller than the electronic conductivity ($>10^{-9}$ S cm^{-1} at RT), which implies that the mass transport of Li^+ is crucial for improving the kinetic issues. Therefore, it presents a possible way to enhance the kinetics of $LiFePO_4$ electrode material through controlling the nanostructure of $LiFePO_4$ with small scale along the b-axis, which may afford the $LiFePO_4$ material excellent performance with high rate capability owing to a shortened lithium ion diffusion path length. Recently, much progress has been made in this respect. Liu et al. [15] adopted a solvothermal method to prepare carbon coated $LiFePO_4$ nanoparticles (~50 nm along the b-axis), which could have a discharge capacity of ~155 mAh g^{-1} at a 0.1 C rate. Manthiram et al. [16] reported that $LiFePO_4$ nanorods (~25 nm along the b-axis) synthesized by a microwave-solvothermal method in tetraethylene glycol solvent, and then networked with conducting multi-walled carbon nanotubes could display discharge capacity of 161 and 130 mAh g^{-1} at 0.1 and 10 C rates, respectively. Vittal et al. [17] adopted solvothermal method to synthesize shaped $LiFePO_4$/C material with ethylene glycol as a solvent, and the b-axis thickness was decreased greatly from 300 to 500 nm (diamond shaped) to ~30 nm (nanoplates) by using an iron precursor of Fe(oxalate) in substitution of $Fe(gluconate)_2$.

In fact, a proper surfactant is crucial for tuning the particle size and morphology owing to the adsorption of surfactant molecules onto the particle surfaces during particle growth. Sodium dodecyl benzene sulfonate (SDBS), which serves as an anionic surfactant has been extensively investigated for synthesis of different nanostructures in the past few years. For examples, Qian et al. [18] reported that uniform tellurium single crystalline nanorods with diameters of 14 nm and lengths of 300 nm were prepared through reduction of $[TeS_4]^{2-}$ by SO_3^{2-} with the use of SDBS, and that the Te nanorods with various diameters could be prepared by carefully adjusting the concentration of SDBS. Chen et al. [19] utilized a hydrothermal method to synthesize $BiVO_4$ nanosheets with thicknesses of 10–40 nm in the presence of SDBS as a morphology-directing template.

In this study, we have respectively prepared $LiFePO_4$ nanoparticles, nanorods and nanoplates with controllable b-axis thickness through tuning the concentration of surfactant SDBS in a hydrothermal way. Experiments show that by increasing concentration of SDBS from 0.0006 M to 0.003 M, the $LiFePO_4$ morphology evolves from nanorods to nanoplate assemblies, while in the absence of SDBS, only nanoparticles were obtained. The three samples with different nanostructures were carbon coated through post-heat treatment. When used as cathode materials in lithium-ion batteries, the $LiFePO_4$/C nanoplates showed enhanced electrochemical performances compared with the $LiFePO_4$/C nanoparticles and nanorods, which demonstrates that a shortening of the lithium ion diffusion path lengths along the b-axis is an effective way to improve the electrochemical properties of $LiFePO_4$ nanomaterials.

2. Experimental

In this work, all chemicals were used as purchased without further purification.

2.1. Preparation of $LiFePO_4$/C samples

The $LiFePO_4$ nanoplates were prepared by a hydrothermal process. The reactants were $LiOH{\cdot}H_2O$, $FeSO_4{\cdot}7H_2O$, H_3PO_4, L(+)-ascorbic acid and sodium dodecyl benzene sulfonate (SDBS, $C_{18}H_{29}SO_3Na$) (AR, Shanghai Chemical Reagents Corporation, China) in a stoichiometric ratio 3:1:1:0.5:0.2. First, $FeSO_4$ (0.015 M), H_3PO_4 (0.015 M), LiOH (0.045 M) and SDBS (0.003 M) aqueous solutions were mixed in 40 mL of distilled water with stirring, and then the mixture was transferred to a 50 mL Teflon-lined stainless steel autoclave and heated at 170 °C for 24 h. After the hydrothermal reaction, the autoclave was cooled to room temperature and the resulting precipitate was filtered, washed and dried at 60 °C for 12 h.

For the synthesis of $LiFePO_4$ nanorods, the procedure was identical except that the concentration of SDBS was reduced by a factor of five. The synthesis process for the $LiFePO_4$ nanoparticles was also identical except SDBS was absent from the reaction solution.

The prepared $LiFePO_4$ was modified with carbon coating through post-heat treatment. Sucrose (AR, Shanghai Chemical Reagents Corporation, China) in a 10:100 weight ratio to $LiFePO_4$ nanoparticles, nanorods and nanoplates was initially dissolved in distilled water to form a transparent solution, with a liquid–solid ratio of 2:1 (mL:g), then mixed with the $LiFePO_4$ materials at room temperature using an ultrasonic device operated at 250 W and 40 kHz (KQ3200E, Kunshan Ultrasonic Instruments Corporation, China) for 20 min to form a uniform slurry. The slurry samples were dried at 90 °C for 12 h to remove the excess water, and the final precursors were obtained. The precursors were first heated to 350 °C for 4 h (heating rate: 4.0 °C min^{-1}) and then to 650 °C for 9 h (2.0 °C min^{-1}) in a tube furnace with a N_2 atmosphere.

For convenience, the carbon coated $LiFePO_4$ nanoparticle, nanorod and nanoplate samples will be referred to as LFP/C nanoparticles, nanorods and nanoplates, respectively.

2.2. Characterization of the samples

The composition and phase purity of the prepared samples were examined by X-ray diffraction (XRD) with a D/max-γB X-ray diffractometer (Shimadzu International Trading Corporation, Japan) utilizing a Cu Kα radiation source ($\lambda = 0.15406$ nm) operated at 40 kV and 80 mA. Field-emission scanning electron microscopy (FESEM) measurements were carried out with a field-emission microscope (JEOL-7500B, JEOL Limited Corporation, Japan) operated at an acceleration voltage of 5 kV. Transmission electron microscopy (TEM) images and high-resolution TEM images of the samples were taken with an H-800 (Hitachi Limited Corporation, Japan) and JEOL-2010 (JEOL Limited Corporation, Japan), respectively, operated at accelerating voltage of 200 kV each. The carbon content in the samples was tested using a Perkin–Elmer Series II CHNS/O (USA) elemental analyzer.

2.3. Electrochemical measurements

The cathode was prepared by mixing 80 wt% active material, 15 wt% acetylene black (Beijing Chemical Reagents Corporation, China) and 5 wt% polyvinylidene fluoride (PVDF, Shanghai Chemical Reagents Corporation, China) as a binder in a solvent of *N*-methyl-2-pyrrolidone (NMP, Shanghai Chemical Reagents Corporation, China) to form a homogeneous slurry. The mixed slurry was then cast onto aluminum foil with the slurry thickness controlled. After the evaporation of the solvent at 60 °C for 2 h in air, the cathode was roll-pressed and cut into pellets of required size for coin-cell fabrication, the pellets were further dried under high vacuum at 120 °C for 5 h.

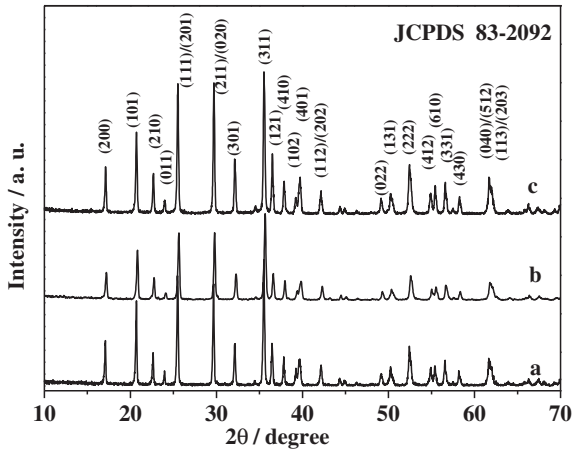

Fig. 1. XRD patterns of LFP/C nanoparticles (a), nanorods (b) and nanoplates (c).

The thickness of the electrode material on aluminum foil was about 28 μm. Lithium foil (Energy Lithium Limited Corporation, China) was used as the anode. The liquid electrolyte utilized was 1 mol L^{-1} $LiPF_6$ in a 1:1 (volume) mixture of ethylene carbonate (EC) and dimethyl carbonate (DMC), and the separator was a polypropylene membrane with micro-pores (Celgard 2400). The coin-type cells (CR2032) were assembled in an Ar-filled dry glove box. The galvanostatic charge–discharge experiment was conducted using a battery testing system (BTS-5V/10 mA, Neware Technology Limited Corporation, China) from 2.5 to 4.2 V (versus Li^+/Li) at room temperature. Cyclic voltammetry (CV) was performed at scan rates of 0.05–0.5 mV s^{-1} from 2.5 to 4.2 V (versus Li^+/Li) on an electrochemical workstation (CHI-660D, Shanghai Chenhua Instrument Limited Corporation, China). In electrochemical impedance spectroscopic (EIS) measurements, the excitation potential applied to the cells was 5 mV and the frequency ranged from 100 kHz to 10 mHz.

3. Results and discussion

The XRD patterns of the LFP/C nanoparticles, nanorods and nanoplates are shown in Fig. 1. The XRD patterns clearly show the single-phase structure of LFP/C without any observable impurity phase (such as Li_3PO_4 and $Li_3Fe_2(PO_4)_3$). All of the peaks in the XRD patterns could be indexed to an orthorhombic space group, *Pnma* (JCPDS Card No. 83-2092).

Fig. 2 depicts the FESEM and TEM images of LFP/C synthesized with different concentrations of SDBS. As shown in Fig. 2a and b,

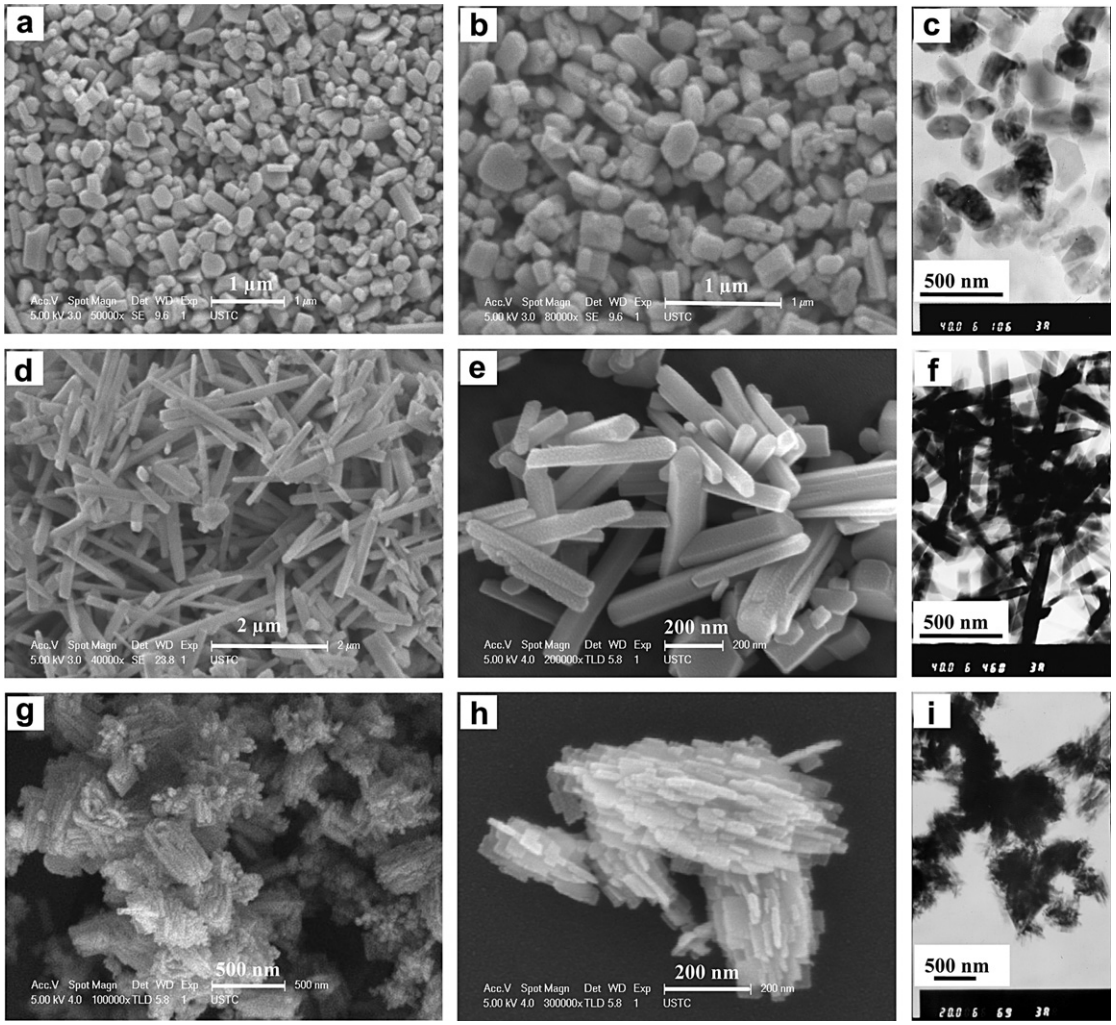

Fig. 2. FESEM images of LFP/C nanoparticles (a, b), nanorods (d, e) and nanoplates (g, h). Also shown are the TEM images; parts (c), (f) and (i) correspond to parts (a), (d), and (g), respectively.

the LFP/C sample composed of uniform nanoparticles was achieved by the hydrothermal synthesis in the absence of SDBS aqueous solution, followed by heat treatment. The average size of the nanoparticles is ~200 nm, which is confirmed by the TEM image shown in Fig. 2c. Fig. 2d–f show LFP/C nanorods obtained with the low concentration of SDBS (0.0006 M). The nanorods have a diameter of 90 nm and a length in the range of 200 nm to 1 μm (Fig. 2d and e). When a higher concentration of SDBS (0.003 M) was used, LFP/C nanoplate assemblies were prepared as shown in Fig. 2g–i. The parallel assembled LFP/C nanoplates have a very thin thickness of ~20 nm, a length in the range of 50–200 nm and a width of ~50 nm.

Further insight into the morphology and crystal growth of the LFP/C nanorods and nanoplates has been gained by high-resolution TEM. Fig. 3a shows the HRTEM image of a single LFP/C nanorod. From the HRTEM image and the inserted selected area electron diffraction (SAED) patterns shown in Fig. 3b (corresponding to the area marked by a circle in Fig. 3a), the interplanar spacings of 1.03 nm and 0.47 nm correspond to the (100) and (001) lattice planes, respectively, demonstrating that the LFP/C nanorods grow preferentially along the [100] direction. Similarly, the HRTEM images and SAED in Fig. 3c and d indicate that the large plane of the LFP/C nanoplates lies in the ac plane, viewed along the b direction. For LFP/C nanorods and nanoplates, the lengths along b-axis are 90 nm and 20 nm, respectively. Fig. 3b and d show uniform carbon coating (amorphous region) with a thickness of ~2 nm on the surface of LFP/C nanorods and nanoplates in the crystalline fringe region. And elemental analysis indicates that the amount of carbon in the LFP/C nanoparticles, nanorods and nanoplates is about 2.13%, 2.22% and 2.25%, respectively, which results from the decomposition of the ascorbic acid and sucrose.

As shown above, with the increasing concentration of SDBS, the $LiFePO_4$ morphology evolves from nanorods to nanoplates. $LiFePO_4$ nanorods grow fast along the [100] direction when the concentration of SDBS is low in the precursor solution. When the SDBS concentration is increased, more SDBS preferentially adsorbs on the (100) plane of $LiFePO_4$ and the growth of the $LiFePO_4$ nanocrystallite along the [100] is partially suppressed. However, the $LiFePO_4$ nanocrystallites can still grow sideways along [001] direction. Therefore, as the SDBS concentration increases, the average aspect ratio (height/width) of $LiFePO_4$ nanorods decreases. Finally, two-dimensional (ac plane) $LiFePO_4$ nanoplates are formed. It is obvious that the length along the [100] direction decreases from ~200 nm (Fig. 2d and e) to ~50 nm (Fig. 3c). As a result, the $LiFePO_4$ morphology evolves from one-dimensional nanorods to two-dimensional nanoplates. Similar observations have been reported by Cao et al. on the morphology conversion from ZnO nanorods to nanoplates [20].

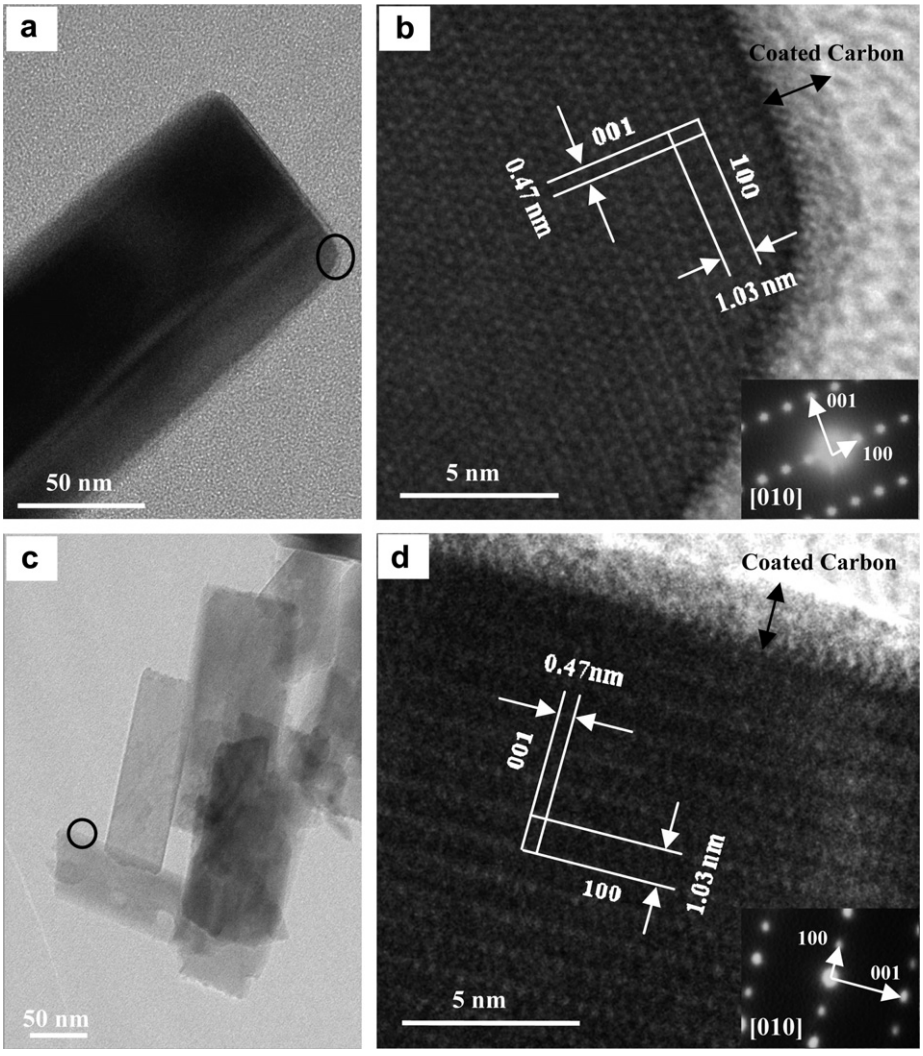

Fig. 3. HRTEM images of LFP/C nanorods (a, b) and nanoplates (c, d). Corresponding SAED patterns are inserted in the bottom right corners.

The electrochemical performance of LFP/C composite materials was investigated with a lithium intercalation/extraction process. Fig. 4 shows the charge–discharge curves of the LFP/C nanoparticles, nanorods and nanoplates with various rates from 0.1 to 10 C between 2.5 and 4.2 V. The comparison for the charge–discharge curves indicates that the LFP/C nanoparticles have the shortest charge–discharge plateau among the samples at all discharge rates. The coulombic efficiencies of the first cycles are 91.4%, 93.6% and 97.3% and the first discharge capacities are 145.3, 149.0 and 162.9 mAh g^{-1} at a 0.1 C rate for LFP/C nanoparticles, nanorods and nanoplates, respectively. Furthermore, the discharge capacities are 79.3, 100.6 and 129.5 mAh g^{-1} at 5 C rate, and 33.8, 61.3 and 107.9 mAh g^{-1} at 10 C rate for LFP/C nanoparticles, nanorods and nanoplates, respectively.

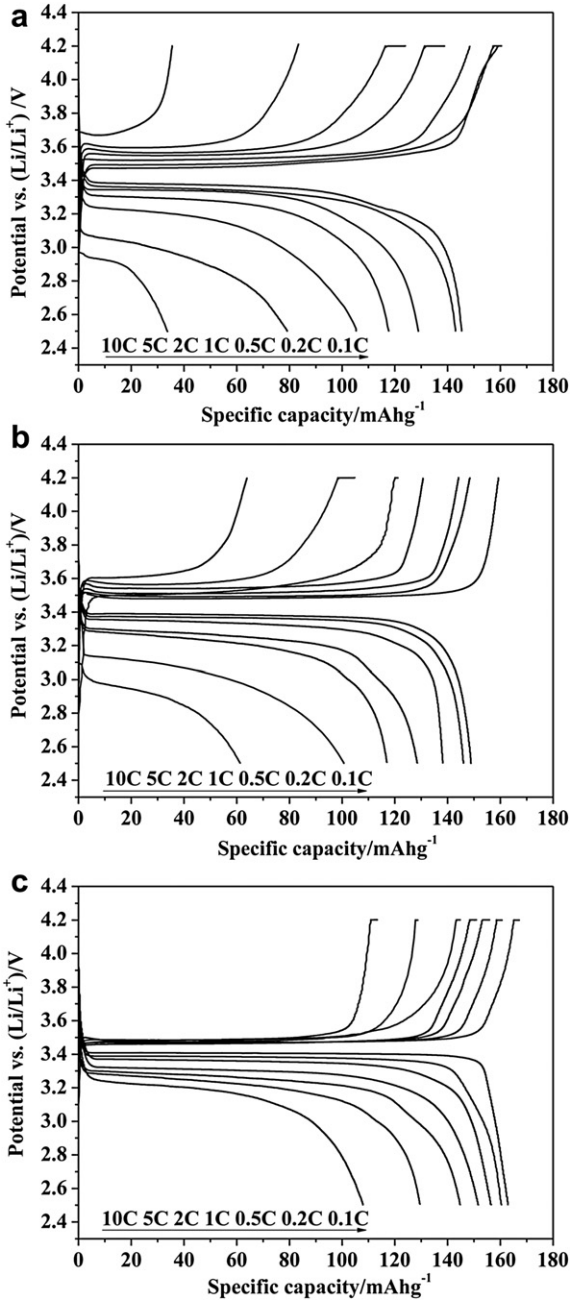

Fig. 4. The initial charge–discharge curves of the LFP/C materials in the potential range of 2.5–4.2 V at various current rates (here 1 C refers to a capacity of 170 mA g^{-1} in an hour): nanoparticles (a), nanorods (b) and nanoplates (c).

Fig. 5 exhibits a comparison of the discharge capacities for LFP/C nanoparticles, nanorods and nanoplates over limited cycling at different C-rates. The discharge capacities of the three samples remain stable and decrease as expected with an increased discharge rate. Compared with that of LFP/C nanoparticles and nanorods, the discharge capacity of LFP/C nanoplates is greatly enhanced at rates from 0.1 C to 10 C, especially at higher current rates. When the current density is decreased from 10 C to 0.1 C at the end of cycling, the capacities of the three samples match their initial discharge capacities (144.9, 148.0 and 161.6 mAh g^{-1} for LFP/C nanoparticles, nanorods and nanoplates, respectively), which may be mainly ascribed to the good electrochemical reversibility and structural stability of phospho-olivine $LiFePO_4$ [1]. Compared with LFP/C nanorods (90 nm along b-axis), LFP/C nanoplates (20 nm thickness along b-axis) show better rate capability. There may be two reasons for the improvements of rate capability. One is attributed to their smaller size along the [010] direction for enhancing the lithium ion diffusion rate [21]. The other may be due to the increase of surface area of (010) plane which is active for Li^+ intercalation/extraction [22]. LFP/C nanoplates with large surface area of (010) plane have a low interfacial charge-transfer resistance of Li^+ intercalation/extraction (shown in Fig. 7a), which would greatly contribute to enhancing the rate capability. The Li-ion diffusion coefficients of the samples will be discussed later.

The influence of morphology on the electrochemical properties of LFP/C nanomaterials was further investigated using cyclic voltammetry. The LFP/C nanoparticle, nanorod and nanoplate samples were tested at a scanning rate of 0.05 mV s^{-1} between the voltage limit of 2.5 and 4.2 V (versus Li^+/Li) and the CV profiles of them are shown in Fig. 6. A pair of anodic and cathodic peaks, which correspond to the two-phase intercalation/extraction of Li^+ ions involving an Fe^{2+}/Fe^{3+} redox couple, is observed. The LFP/C nanoplates exhibit an anodic peak at 3.52 V and a corresponding cathodic response at 3.33 V. The separation potential of LFP/C nanoplates is 0.19 V, whereas those of the LFP/C nanorods and nanoparticles are 0.26 V and 0.34 V, respectively. The more symmetric and spiculate peak profile for LFP/C nanoplates indicates a reversible elctrochemical reaction during lithium ion insertion and extraction [23]. Compared with LFP/C nanoparticles and nanorods, the LFP/C nanoplates can enhance the electrochemical reaction kinetics and reduce the polarization.

Electrochemical impedance spectroscopy was measured in the full charge state. Fig. 7a shows Nyquist plots of LFP/C nanoparticles,

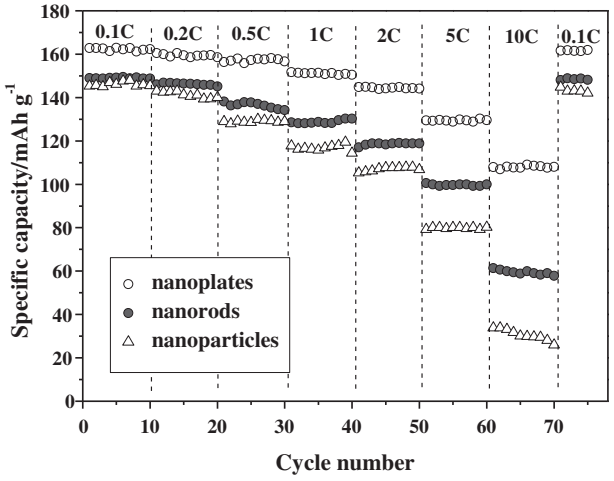

Fig. 5. The rate and cycling performances of LFP/C nanoparticles, nanorods and nanoplates. The cells were charged at a rate of 0.2 C to ensure identical conditions for each discharge.

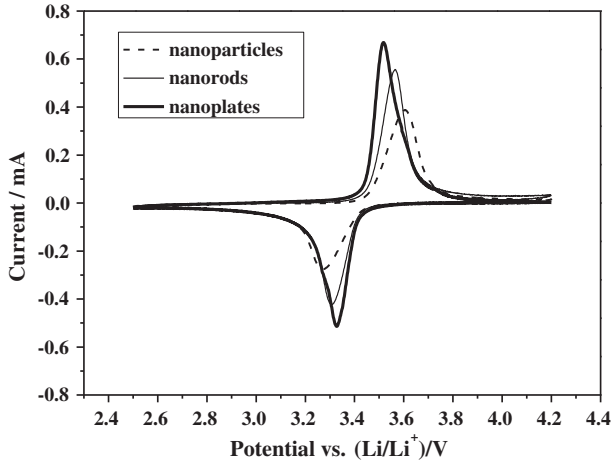

Fig. 6. Cyclic voltammograms for LFP/C nanoparticles, nanorods and nanoplates in the first cycle at a scan rate of 0.05 mV s^{-1} between the potential limits of 2.5 and 4.2 V (versus Li^+/Li).

nanorods and nanoplates in the frequency range between 100 kHz and 10 mHz. Both EIS profiles exhibit a semicircle in the high frequency region and a straight line in the low frequency region. The intercept impedance on the real axis corresponds to the solution resistance (R_e). The numerical value of the diameter of the semicircle on the Zreal axis is approximately equal to the charge-transfer resistance (R_{ct}). The low frequency region of the straight line is attributed to the Warburg diffusion of the lithium ions into the bulk electrode material. From Fig. 7a, the R_{ct} of LFP/C nanoplates (48.7 Ω) is much smaller than that of LFP/C nanorods (93.1 Ω) and nanoparticles (142.5 Ω).

Fig. 7b shows the relationship between Z_{Re} and square root of frequency ($\omega^{-1/2}$) in the low frequency region. Using Equation (1), it is found that the Warburg impedance coefficient (σ_w) of LFP/C nanoplates is 5.54 Ω cm^2 $s^{-1/2}$. This value is low in comparison to the LFP/C nanoparticles (16.80 Ω cm^2 $s^{-1/2}$) and nanorods (12.53 Ω cm^2 $s^{-1/2}$).

$$Z_{Re} = R_e + R_{ct} + \sigma_w \omega^{-1/2} \quad (1)$$

$$D = R^2T^2/2A^2n^4F^4C^2\sigma_w^2 \quad (2)$$

Equation (2) can be used to calculate the Li-ion diffusion coefficient, D (cm^2 s^{-1}). R is gas constant (8.314 J mol^{-1} K^{-1}), T is the absolute temperature (K), A is the electrode area (cm^2), n is the number of electrons involved in the redox process (1 in our case), C is the shuttle concentration (7.69×10^{-3} mol cm^{-3}) and F is the Faraday constant (96486 C mol^{-1}). The Li-ion diffusion coefficients of LFP/C nanoparticles, nanorods and nanoplates are calculated to be 1.66×10^{-12}, 2.99×10^{-12} and 1.64×10^{-11} cm^2 s^{-1}, respectively. The values were comparable to previously reported data (e.g. 10^{-15}–10^{-11} cm^2 s^{-1} by EIS, 10^{-15}–10^{-12} cm^2 s^{-1} by PITT) [24,25]. The results manifest that the nanoplates with the smallest size in the b-axis have the highest Li-ion diffusion coefficient. The result is in good agreement with the reported data by Liu et al. [15]. As for olivine $LiFePO_4$, bi-phasic phase transition takes place during insertion and extraction of Li^+. Thereby, phase-boundary movements might occur within LFP/C materials and hence, the rate of phase-boundary movement is significantly affected by the crystal thickness and shape. The bi-phasic reaction rate of LFP/C materials can be enhanced by reducing the crystal dimension along the b-axis [17,26]. Lithium ions need to transport shorter distances before reaching the phase boundaries in the $LiFePO_4$ nanoplates than in the nanorods and the nanoparticles. Therefore, the overall lithium

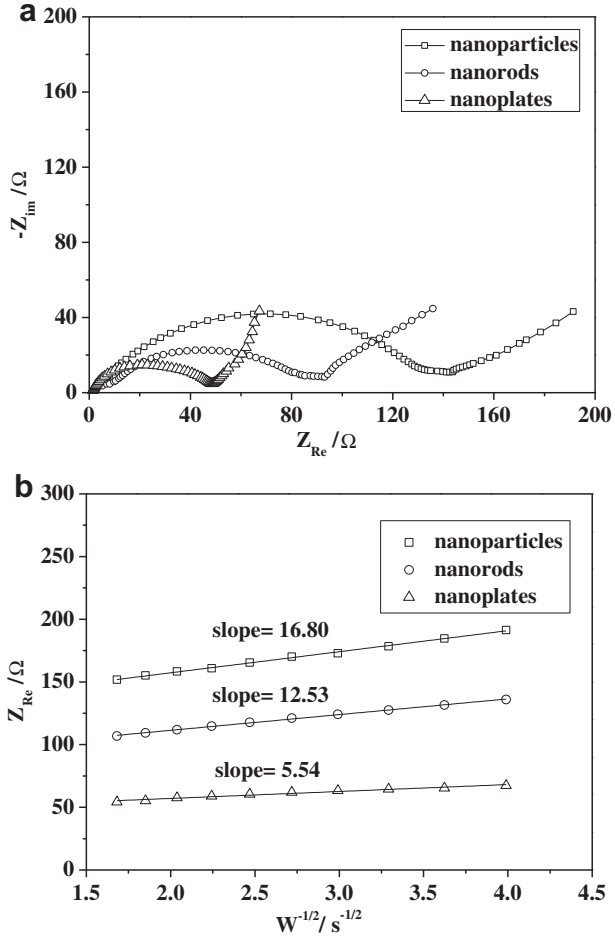

Fig. 7. (a) Electrochemical impedance spectroscopy (EIS) results of LFP/C nanoparticles, nanorods and nanoplates at full charge in the frequency range between 100 kHz and 10 mHz. (b) The relationship between Z_{Re} and $\omega^{-1/2}$ at low frequency.

ion diffusion dynamics in the $LiFePO_4$ nanoplates is faster than that in the nanorods and the nanoparticles.

By applying the Randles Sevcik equation [27], a similar result was obtained by CV, and Li-ion diffusion coefficients of LFP/C nanoparticles, nanorods and nanoplates are calculated to be 5.62×10^{-10}, 1.08×10^{-9} and 2.01×10^{-9} cm^2 s^{-1}, respectively. More details can be observed in Fig. S1.

In general, LFP/C nanoparticles, nanorods and nanoplates with controllable b-axis thickness have been synthesized respectively by a hydrothermal way with different concentrations of SDBS. The LFP/C nanoplates with the short b-axis thickness have the excellent electrochemical performance among the LFP/C nanocomposites. And the superior electrochemical property is ascribed to the short lithium ion diffusion path (b-axis) and high Li-ion diffusion coefficient.

4. Conclusions

In summary, we have adopted a hydrothermal route to synthesize LFP/C nanoparticles, nanorods and nanoplates with controllable b-axis thickness just by altering the concentration of SDBS. It has been found that the b-axis thickness has significant effects on the electrochemical performance of the LFP/C nanocomposites when used in the LIBs. The $LiFePO_4$/C nanoparticles (200 nm in size) and nanorods (90 nm in diameter and 200 nm–1 μm in length) exhibit poor electrochemical

performances, e.g. low charge/discharge capacity and high charge-transfer resistance. With a decrease of the crystallite size in the b-axis by altering the concentration of SDBS, the LFP/C nanoplates exhibit significantly improved electrochemical performance compared with those with larger crystal sizes in the b-axis. The nanoplates exhibit improved charge/discharge capacity close to the theoretical capacity of the $LiFePO_4$ materials along with enhanced cycling stability, which shows that reducing the crystallite size in the b-axis and increasing the surface area of (010) plane can shorten lithium ion diffusion path and increase the electrode reaction. The obtained LFP/C nanoplates with superior electrochemical performance are anticipated to meet the industrial needs for electric vehicles (EV), hybrid electric vehicles (HEV), and other mobile or portable electric devices.

Acknowledgments

This work was supported by the National Natural Science Foundation of China (NSFC Grants 20871038, 20976033 and 21176054), the Fundamental Research Funds for the Central Universities (2010HGZY0012) and the Education Department of Anhui Provincial Government (TD200702).

Appendix A. Supplementary data

Supplementary information related to this article can be found at http://dx.doi.org/10.1016/j.jpowsour.2012.07.128.

References

[1] A.K. Padhi, K.S. Nanjundawamy, J.B. Goodenough, J. Electrochem. Soc. 1 (1997) 1188–1194.
[2] D.D. Macneil, Z.H. Lu, Z.H. Chen, J.R. Dahn, J. Power Sources 108 (2002) 8–14.
[3] H. Huang, S.C. Yin, L.F. Nazar, Electrochem. Solid-State Lett. 4 (2001) A170–A172.
[4] R. Amin, P. Balaya, J. Maier, Electrochem. Solid-State Lett. 10 (2007) A13–A16.
[5] W. Ojczyk, J. Marzec, K. Świerczek, W. Zajac, M. Molenda, R. Dziembaj, J. Molenda, J. Power Sources 173 (2007) 700–706.
[6] Y.S. Hu, Y.G. Guo, R. Dominko, M. Gaberscek, J. Jamnik, J. Maier, Adv. Mater. 19 (2007) 1963–1966.
[7] A.K. Padhi, K.S. Nanjundaswamy, C. Masquelier, S. Okada, J.B. Goodenough, J. Electrochem. Soc. 144 (1997) 1609–1613.
[8] J. Moskon, R. Dominko, R.C. Korosec, M. Gaberscek, J. Jamnik, J. Power Sources 174 (2007) 683–688.
[9] Y.H. Huang, J.B. Goodenough, Chem. Mater. 20 (2008) 7237–7241.
[10] S.Y. Chung, J.T. Bloking, Y.M. Chiang, Nat. Mater. 1 (2002) 123–128.
[11] B. Pei, Q. Wang, W.X. Zhang, Z.H. Yang, M. Chen, Electrochim. Acta 56 (2011) 5667–5672.
[12] J. Hong, C.S. Wang, X. Chen, S. Upreti, M.S. Whittingham, Electrochem. Solid-State Lett. 12 (2009) A33–A38.
[13] M.S. Islam, D.J. Driscoll, C.A.J. Fisher, P.R. Slater, Chem. Mater. 17 (2005) 5085–5092.
[14] M. Gaberscek, R. Dominko, J. Jamnik, Electrochem. Commun. 9 (2007) 2778–2783.
[15] S.L. Yang, X.F. Zhou, J.G. Zhang, Z.P. Liu, J. Mater. Chem. 20 (2010) 8086–8091.
[16] T. Muraliganth, A.V. Murugan, A. Manthiram, J. Mater. Chem. 18 (2008) 5661–5668.
[17] K. Saravanan, P. Balaya, M.V. Reddy, B.V.R. Chowdari, J.J. Vittal, Energy Environ. Sci. 3 (2010) 457–464.
[18] Z.P. Liu, Z.K. Hu, Q. Xie, B.J. Yang, J. Wu, Y.T. Qian, J. Mater. Chem. 13 (2003) 159–162.
[19] L. Zhang, D.R. Chen, X.L. Jiao, J. Phys. Chem. B 110 (2006) 2668–2673.
[20] B.Q. Cao, W.P. Cai, J. Phys. Chem. C 112 (2008) 680–685.
[21] K. Saravanan, M.V. Reddy, P. Balaya, B.V.R. Chowdari, J.J. Vittal, J. Mater. Chem. 19 (2009) 605–610.
[22] D.H. Kim, J. Kim, Electrochem. Solid-State Lett. 9 (2006) A439–A442.
[23] H.C. Shin, W.I. Cho, H. Jang, J. Power Sources 159 (2006) 1383–1388.
[24] L.X. Li, X.C. Tang, H.T. Liu, Y. Qu, Z.G. Lu, Electrochim. Acta 56 (2010) 995–999.
[25] J. Xie, N. Imanishi, T. Zhang, A. Hirano, Y. Takeda, O. Yamamoto, Electrochim. Acta 54 (2009) 4631–4637.
[26] J. Chen, L.M. Yan, B.H. Yue, J. Power Sources 209 (2012) 7–14.
[27] Y.D. Cho, G.T.K. Fey, H.M. Kao, J. Power Sources 189 (2009) 256–262.